Three-dimensional (3D) Simulation of Micro-Void Development within Large Scale Polymer Composite Deposition Beads

Aigbe Awenlimobor⁺, Douglas E. Smith⁺, Zhaogui Wang^{*}, Chenjun Luo^{*}

⁺ Department of Mechanical Engineering, Baylor University, Waco, TX 76798 * Department of Mechanical Engineering, Dalian Maritime University, Dalian, China, 116026

⁺Corresponding author. Email: aigbe_awenlimobor1@baylor.edu

Abstract

Structural integrity and quality of short fiber composite parts produced by Big Area Additive Manufacturing (BAAM) are largely affected by inherent bead microstructural features such as voids. Unfortunately, our understanding of void nucleation and evolution during polymer deposition process is lacking. Flow modeling focused on the associated microstructural formation provides a means for better understanding the process-structure-properties relations in large area extrusion deposition additive manufacturing of fiber reinforced composites. Our prior computational effort that investigated mechanisms that may promote micro-void formation was based on 2-dimensional planar models of a single ellipsoidal fiber motion in purely viscous polymer extrusion/deposition flow through a BAAM nozzle. Here we present a 3D finite element modelling approach to simulate single fiber out-of-plane rotations utilizing velocity and velocity gradient values computed along streamlines obtained from a 3D extrusion/deposition simulation of the BAAM polymer deposition process. The pressure distribution on the fiber's surface along the flow path provides new insight into potential micro-void nucleation mechanism. Results show low pressure regions occur near the fiber's surface which varies across the printed bead and through its thickness.

Introduction

Short fiber reinforced thermoplastics exhibit superior stiffness-to-weight ratio as compared to their neat polymer alternatives, and thus haven seen continuous implementations in Large Area extrusion deposition Additive Manufacturing (LAAM). The material flow in the nozzle and subsequent deposition is crucial for determining the microstructural formations of the deposited composites, that directly influence the material behaviors of the solidified LAAM-printed parts. Micro voids within the LAAM bead are one such formation that has a significant influence on part integrity. Void nucleation has been identified to be dependent on both external factors and inherent fluid/flow properties. Various literature suggests possible sources that could instigate void nucleation including residual stresses, air entrapment, and volatile induction. Prior research has developed comprehensive mathematical models for volatile-induced void formation and void growth. One notable work by Roychowdhury et. al [1], in his model development, established dependence of the critical radius of nucleation and nucleation rate on the vapor pressure and pressure of surrounding fluid.

Despite prior research efforts, definitive explanation for the formation and growth of microstructural voids remains inadequate, especially the effect of suspended fibers on the nucleation mechanism in LAAM polymer composite deposition. Vaxman et al. [2] suggests fiber aspect ratio dependent pressure localization as a contributing mechanism to void formation and showed that void nucleation is influenced by the melt flow shear rate, flow temperature and viscosity which itself is affected by the fiber distribution and alignment. Other contributing factors identified by [3] that affects void formation includes the dissimilar fiber-matrix coefficient of thermal expansion, the die swell/expansion of the free extrudate and differential cooling rate between the bead's external surface and core regions.

This paper presents a computational method for understanding the mechanisms that may promote void formation. Based on a multiscale model methodology, we developed a three-dimensional (3D) Newtonian flow single ellipsoidal rigid fiber finite element model to simulate out-of-plane rotations. In this approach, velocity and velocity gradient values computed along 3D streamlines are obtained from a macro-scale 3D extrusion/deposition simulation of the BAAM polymer deposition process. At the micro scale, the fiber's linear and angular velocities that result in zero net hydrodynamic force and torque on the fiber surface are computed based on Jeffery's assumption and the fiber's position are updated based on an explicit numerical algorithm. The rigor of adaptive remeshing is overcome by updating the fluid boundary conditions with respect to the fiber's local orientation, while keeping a fixed mesh geometry during the transient analysis. The pressure distribution on the fiber's surface along the flow path especially during die swell expansion at the nozzle exit provides new insight into mechanisms that could promote micro-void nucleation within the printed beads. Model validation is achieved based by benchmarking results for a planar shear flow with analytical solutions developed by Jeffery [4]. Results show low pressure regions near the fiber's surface which varies across the printed bead as well as through its thickness.

Methodology

Macro Model - 3D Extrusion/Deposition Flow

The flow domain for the macro model simulation is the polymer composite melt flow region within the nozzle and the subsequent 90-degree turning deposition onto the material substrate. The nozzle internal geometry is defined based on the design of a Strangpresse Model 19 (Strangpresse, LLC, Youngstown, Ohio, USA) single screw extruder nozzle, which is designed specifically for LAAM processes (cf. Figure 1). We note that the free surface of the deposition flow is difficult to compute, especially for a steady state flow. In prior research, the flow model was evaluated in 2D [4-7], where the associated fiber-induced fiber orientation was computed in a one-way weakly coupled [5] and a fully coupled [4,6,7] flow/orientation analysis. In the present study, we first consider a fully solved 2D planar extrusion deposition approximation for a CF-ABS composite flow [7] as shown in Figure 2, where the boundary conditions of the 2D flow are defined in Figure 2(a) and the computed flow velocity contour v_v is shown in Figure 2 (d). Then, we revolve the nozzle geometry with vertical extrudate (i.e., the flow in Ω_1 and Ω_2 in Figure 2(a)) around the center line of the nozzle (cf. Figure 1) by 180 degrees to generate a 3D flow domain such that the 3D deposition flow domain is obtained by extruding the cross-section area of bead cross section portion of Ω_2 along the direction of deposition, as appearing in Figure 2 (b). which provides an approximate 3D flow domain at a significant computational cost savings as compared to iterative solution methods for determining the shape of the free surface.

In this model, the average inlet velocity is defined as 6.25 mm/s, yielding an average exit velocity of 100 mm/s (computed based on flow rate conservation), which is a typical printing speed employed in LAAM applications [5,7]. The internal nozzle boundary is set as a no-slip wall boundary condition. The upper free surface of the deposition flow is set as fully developed (fixed through the simulation). In contrast, the front and side surfaces of the deposition flow are set as free surface boundaries. The improved elastic remeshing technique (built-in function in Polyflow) is applied for the surface profiles identifications. The flow end is set such that the normal and tangent force of the boundary are zeros. Note, the influence of surface tension is neglected during the computations. In addition, the lower surface boundary of the deposition flow is considered to be perfectly bonded to the print plate immediately after they contacted with each other. To this end, the velocity component along the deposition direction of 100 mm/s is imposed to the bottom surface of the deposition flow, simulating the relative motion between the nozzle and material substrate.

The 3D flow model is solved via ANSYS-Polyflow module (ANSYS Inc., Canonsburg, PA, USA) using a one-way weakly coupled formulation, where the flow is solved assuming a homogeneous melt flow with no fibers. The internal nozzle flow region is meshed with 4-node quadrilateral elements and the free

deposition flow region is meshed with tetrahedral elements to better depict the 3D curvatures of the swelled free surface boundaries. There are a total of 25878 elements with 9084 nodes for the model in this study.

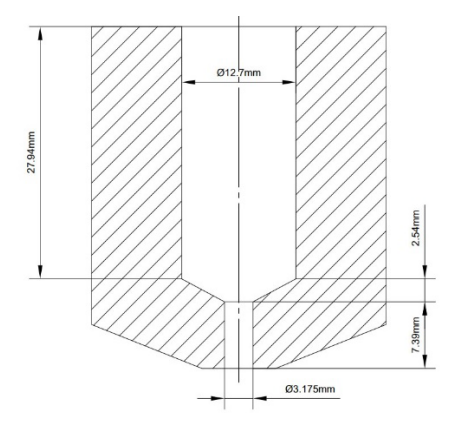


Figure 1: Nozzle internal geometry of a Strangpresse Model 19 single screw extruder. [12]

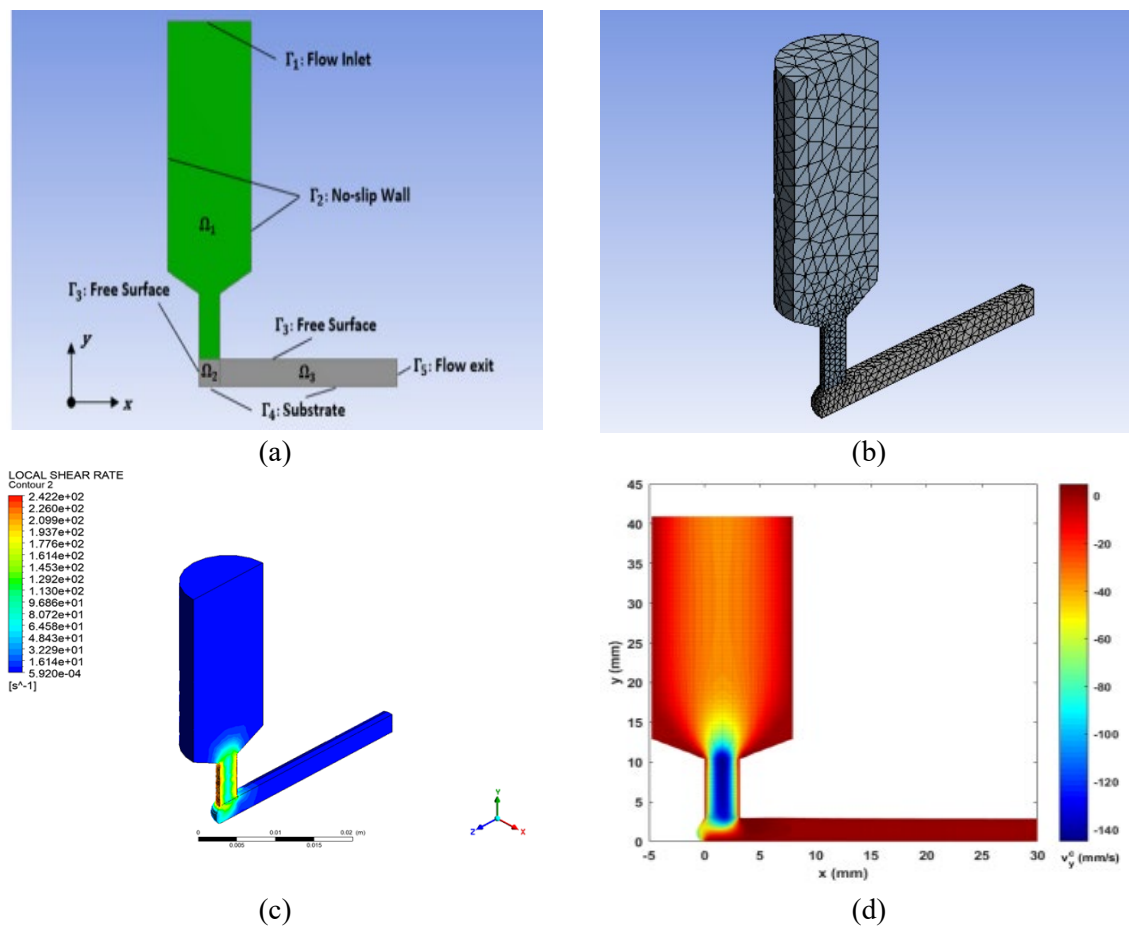


Figure 2: 3D extrusion deposition flow model: (a) Boundary Conditions (b) Mesh geometry of the half-symmetry plane (c) Local shear rates of half-symmetry plane (d) fully-coupled solution of velocity contour v_y .

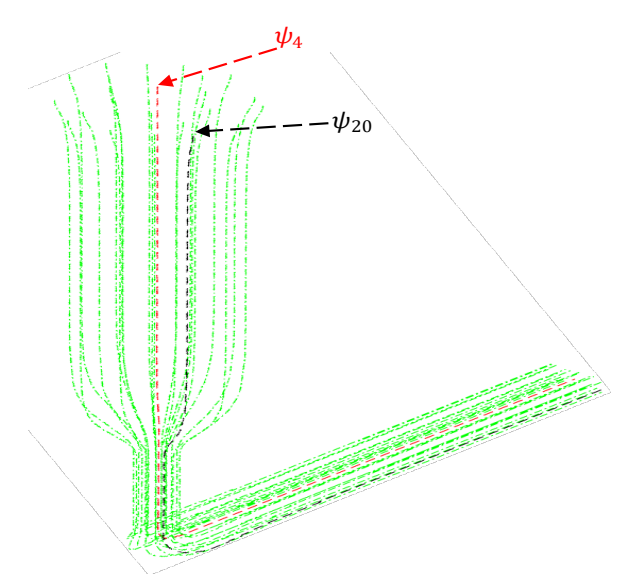


Figure 3: 3D Streamline contours of the BAAM polymer extrusion/deposition simulation highlighting select streamlines (ψ =4 & 20) considered for the single fiber evolution model

Micro-Model – 3D Single Fiber Evolution Model

In the micro-model evaluation, a custom finite element analysis (FEA) code is developed in MATLAB to simulate the quasi-time dependent evolution of a rigid ellipsoidal fiber along 3D streamlines of the BAAM polymer extrusion flow described above. Computed values of the streamline velocities, velocity gradients and pressures obtained from the 3D polymer deposition macro model are supplied as inputs to the single fiber micro model analysis. The governing equations for polymer melt flow in the micromodel are derived from Stokes equation neglecting compressibility, inertia, anisotropic, inhomogeneity and thermal effects, and considering a Newtonian fluid. Similar flow model assumptions and polymer melt properties in the macro model are assumed. The transformed FEA Galerkin weak formulation for mass and momentum conservation used in developing the element stiffness matrices and force vectors in the FEA model are given as:

$$\int_{\Omega^{e}} \underline{\phi}^{e^{T}} \underline{B}^{e} d\Omega^{e} \underline{d}^{e} = 0$$

$$\int_{\Omega^{e}} \underline{B}^{e^{T}} \underline{\mu} \underline{\underline{C}}_{o} \underline{B}^{e} d\Omega^{e} \underline{d}^{e} - \int_{\Omega^{e}} \underline{B}^{e^{T}} \underline{\phi}^{e} d\Omega^{e} \underline{p}^{e} - \int_{\Omega^{e}} \rho \underline{\underline{N}}^{e^{T}} \underline{f} d\Omega^{e} - \int_{\Gamma_{\tau}^{e}} \underline{\underline{N}}^{e^{T}} \underline{\overline{t}} d\Gamma^{e} = 0$$
2

where ρ and μ are the fluid density and dynamic viscosity, $\underline{\phi}^e$ and $\underline{\underline{N}}^e$ are the pressure and velocity shape functions, respectively, $\underline{\underline{B}}^e$ and $\underline{\underline{B}}^e_s$ are strain displacement matrices, $\underline{\underline{d}}^e$ and $\underline{\underline{p}}^e$ are the velocities and pressures degrees of freedom ($\overline{\text{DoF}}$) at their respective element nodes, $\underline{\underline{t}}$ and $\underline{\underline{f}}$ are the element surface tractions and body forces, and Γ^e and Ω^e are element surface and volume domains of integration.

In the micro model, we assume no slip on the fiber surface and no flux across the fiber surface. In the FEA model, three (3) essential boundary conditions are prescribed (cf Figure 4(b)). The streamline velocities and velocity gradients are used to extrapolate the far-field velocities from the macro model onto the fluid boundary $\underline{U}^{\text{BC1}}$.

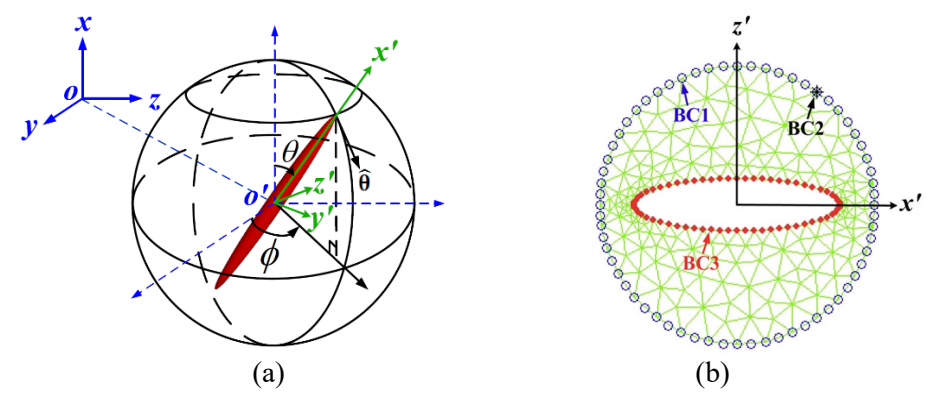


Figure 4: (a) 3D Global and fiber's local reference frame and orientation angle definition (b) Essential boundary conditions (BC1, BC2, and BC3). Image Source [14,15]

To reduce computation time, FEA calculations are performed based on the fiber's local coordinate systems by keeping a constant mesh geometry where velocity boundary conditions are recalculated based on a transformation operation with respect to the fibers axis. The resulting velocities on the fluid boundary may be expressed as

$$\underline{U}^{\text{BC1}} = \underline{R}_{\Omega}^{T} \underline{U}_{\psi} + \underline{R}_{\Omega}^{T} \underline{\nabla}^{T} \underline{U}_{\psi} \underline{R}_{\Omega} \underline{\Delta} \underline{R}^{BC1}$$
3

$$\underline{U}_{\psi} = \begin{bmatrix} u_{\psi} \\ v_{\psi} \\ w_{\psi} \end{bmatrix}, \qquad \underline{\nabla}^{T} = \begin{bmatrix} \partial /_{\partial x} & \partial /_{\partial y} & \partial /_{\partial z} \end{bmatrix}, \qquad \underline{\Delta R} = \begin{bmatrix} \Delta x' \\ \Delta y' \\ \Delta z' \end{bmatrix}$$

where the transformation operation is achieved through a set of fiber rotations based on the Euler's orientation angle thus

$$\underline{\underline{R}}_{\Omega} = \underline{\underline{R}}_{\phi}^{T} \underline{\underline{R}}_{\theta}^{T} \underline{\underline{R}}_{\psi}^{T}$$
 4

In the above,

$$\underline{\underline{R}}_{\phi} = \begin{bmatrix} 1 & 0 & 0 \\ 0 & \cos\phi & \sin\phi \\ 0 & -\sin\phi & \cos\phi \end{bmatrix}, \underline{\underline{R}}_{\theta} = \begin{bmatrix} \cos\theta & \sin\theta & 0 \\ -\sin\theta & \cos\theta & 0 \\ 0 & 0 & 1 \end{bmatrix}, \underline{\underline{R}}_{\psi} = \begin{bmatrix} 1 & 0 & 0 \\ 0 & \cos\psi & \sin\psi \\ 0 & -\sin\psi & \cos\psi \end{bmatrix}$$

The prescribed velocity on the fiber's surface \underline{U}^{BC3} is computed from the fiber's center linear and angular velocities according to the equation of rigid body motion (cf. Equation 5). Likewise, we transform the global velocities into local variables with respect to the fibers local reference axis as:

$$\underline{U}^{\text{BC3}} = \underline{R}_{\Omega}^{T} \underline{U}_{c} + \underline{R}_{\Omega}^{T} \underline{R}_{\dot{\Omega}} \, \underline{\dot{\Omega}} \times \underline{\Delta} \underline{R}^{BC3}$$

where,

$$\underline{\underline{R}}_{\dot{\Omega}} = \begin{bmatrix} 1 & 0 & \cos \theta \\ 0 & -\sin \phi & \sin \theta \cos \phi \\ 0 & \cos \phi & \sin \theta \sin \phi \end{bmatrix}, \qquad \underline{\underline{U}}_{c} = \begin{bmatrix} u_{c} \\ v_{c} \\ w_{c} \end{bmatrix}, \qquad \underline{\dot{\Omega}} = \begin{bmatrix} \dot{\phi} \\ \dot{\theta} \\ \dot{\psi} \end{bmatrix}, \qquad \underline{\underline{\Delta}\underline{R}} = \begin{bmatrix} \Delta x' \\ \Delta y' \\ \Delta z' \end{bmatrix}$$

The pressure point constraint p_{BC2} is prescribed by imposing the far-field streamline pressure p_{ψ} from the macro model simulation result at a node on the fluid surface according to

$$p_{BC2} = p_{\psi} \tag{6}$$

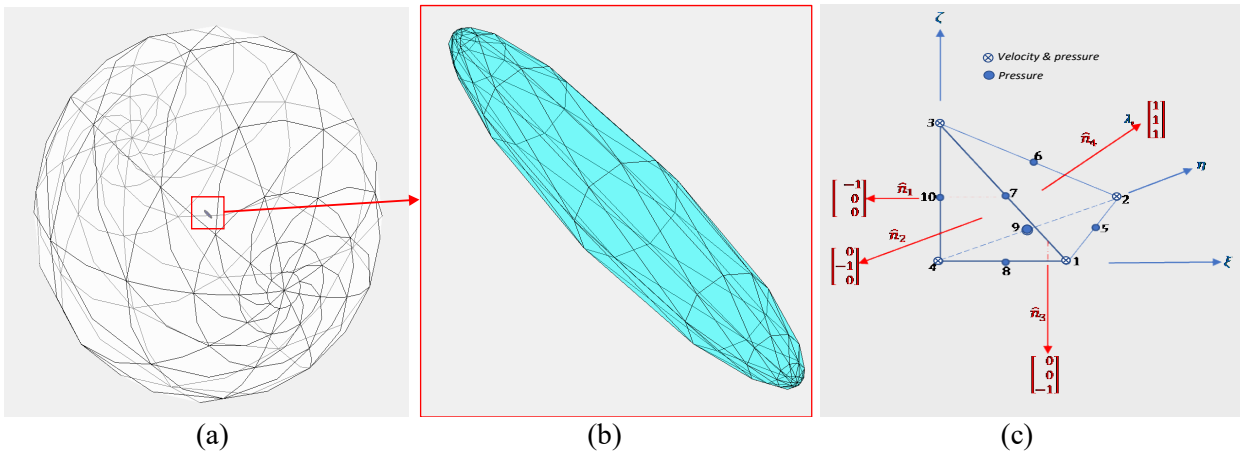


Figure 5: (a) Finite element domain showing mesh geometry for outer boundary, (b) mesh geometry on the fiber surface (c) 3-node tetrahedral element showing velocity and pressure DoF

In the FEA formulation, the element stiffness matrices are derived based on the mixed method with velocities and pressure DoF as the primary nodal variables. The derived element shape functions are quadratic for the velocities and linear for the pressure. We employ quadratic iso-parametric serendipity tetrahedral elements for the analysis with 6 mid-side nodes (3 velocities DoF) and 4 vertex nodes (3 velocities + 1 pressure DoF). We achieve domain discretization by using a radial seed of 28 cell units with a geometric bias of 1.2, an azimuthal seed of 20 cell unit around the half-circumference of the fiber's long axis with a geometric bias of 0.8 towards its midplane and a polar seed of 18 equally spaced cells. For each prism element at the fibers tip, there are 3 tetrahedral element and for each hexahedral element there are 6 tetrahedral elements resulting in a total element of 6804 tetrahedral elements.

We compute the system nodal velocity and pressure degrees of freedom compose the unknown vector U from a solution technique based on partitioning the assembled linear algebraic system of equation of the form [17]

$$\underline{K}\,\underline{U} = \underline{F}$$

 $\underline{\underline{K}} \, \underline{U} = \underline{F}$ into essential and free degrees of freedom (denoted by 'e' & 'f' post subscript respectively). $\underline{\underline{K}}$ is the global system 'stiffness' matrix and F is the associated force vector containing the respective nodal reaction forces and flow rates.

$$\begin{bmatrix} K_{ff} & K_{fe} \\ K_{ef} & K_{ee} \end{bmatrix} \begin{bmatrix} u_f \\ u_e \end{bmatrix} = \begin{bmatrix} F_f \\ F_e \end{bmatrix}$$
 8

The fiber's translational and angular velocities are obtained by zeroing the hydrodynamic forces and torques acting on the fiber's surface due to exertion from the surrounding fluid. This is achieved using a Newton-Raphson (NR) algorithm [14,15] thus

$$\underline{\dot{X}}^{+} = \underline{\dot{X}}^{-} - \underline{J}^{-} \backslash \underline{R}^{-}$$

In the above, \underline{R} is the residual vector containing the fiber's hydrodynamic forces \underline{F}_H and torques \underline{T}_H and $\underline{\dot{X}}$ is the fiber's velocity vector comprising the fiber's translational and rotational velocity vector, i.e. $\underline{R} =$ $[\underline{F}_H \quad \underline{T}_H]^T$ and $\dot{X} = [\dot{X}_C \quad \dot{\Omega}]^T$. The net hydrodynamic forces and torques acting on the fiber are the nodal summation of the force components and the nodal summation of the vector product of the position vectors and force components over the fiber surface, i.e.

$$\underline{F}_{H} = -\sum_{n \in N} \underline{F}_{e,n}^{BC3} \quad , \quad T_{H} = -\sum_{n \in N} \underline{r}_{n} \times \underline{F}_{e,n}^{BC3}$$
 10

The Jacobian \underline{J} for the Newton Raphson iteration is obtained by differentiating the residual vector \underline{R} with respect to the fiber's velocity \underline{X} , which requires differentiating the nodal component forces with respect to the fiber's velocity vector. i.e.

$$J = \frac{\partial R}{\partial \underline{\dot{X}}} = \frac{\partial}{\partial \underline{\dot{X}}} [\underline{F}_H \quad \underline{T}_H]^T = \left[-\sum_{n \in N} \frac{\partial \underline{F}_{\varrho,n}^{BC3}}{\partial \underline{\dot{X}}} \right]^T - \sum_{n \in N} \underline{r}_n \times \frac{\partial \underline{F}_{\varrho,n}^{BC3}}{\partial \underline{\dot{X}}}$$
11

In addition, the velocity derivative of the nodal reaction force based on Newtonian fluid is

$$\frac{\partial \underline{F}_{e}}{\partial \underline{\dot{X}}} = \left(\underline{\underline{K}}_{ee} - \underline{\underline{K}}_{ef} \underline{\underline{K}}_{f}^{-1} \underline{\underline{K}}_{fe}\right) \frac{\partial \underline{u}_{e}}{\partial \underline{\dot{X}}}$$
 12

The global transformation matrix for the fiber's velocities based on its reference frame of axis is given by,

$$\underline{\underline{R}_{\dot{X}}} = \begin{bmatrix} \underline{\underline{R}_{\Omega}} & \underline{\underline{0}} \\ \underline{\underline{0}} & \underline{\underline{R}_{\dot{\Omega}}}\underline{\underline{R}_{\Omega}} \end{bmatrix}$$
13

The quasi-time dependent evolution of the fiber is computed using a fourth order Runge-Kutta iteration algorithm to update the fibers position and orientation.

Model Verification

To validate the FEA model for the single fiber evolution, we compare results of a stationary study for simple shear flow with results obtained from commercial software – COMSOL Multiphysics. In both models, we consider zero initial fiber orientation and angular velocities and zero pressure point constraint at a far field boundary node. We consider a fiber aspect ratio of 6:1, a shear rate of 1 [s⁻¹] in the y-plane. For model validation we consider a rather coarse mesh with a total element of 2916 units. The mesh geometry from the custom FEA software is imported into the COMSOL model for uniformity. A sufficiently large fluid domain size is considered such that the ratio of the far-field radial distance to the fiber's long axis is 20:1

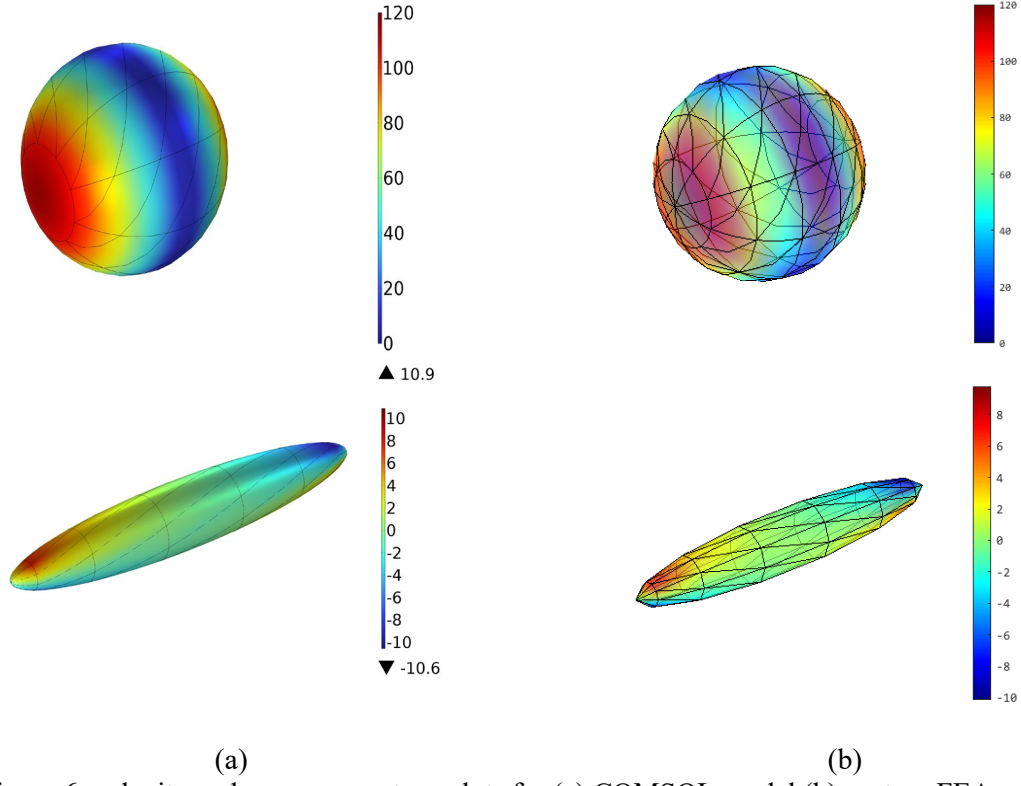


Figure 6: velocity and pressure contour plots for (a) COMSOL model (b) custom FEA model

From the result we see a discrepancy less than 4.7% in the minimum pressure on the fibers surface. For further verification, we benchmark result of orientation angle of the time evolution model for the single fiber along Jefferies orbit and compare to values obtained analytically. The Jefferies equation are developed based on zero-torque acting on a rigid ellipsoidal fiber suspension in a homogenous simple shear Newtonian flow and assuming the fiber translates with the same translational velocities of the undisturbed surrounding fluid [3]. Based on these assumptions, Jeffery's analytical relations for the fiber's angular velocities are presented in Equation 11 below.

$$\dot{\phi}(t) = \frac{\dot{\gamma}}{2} [\lambda \cos 2\phi + 1], \ \dot{\theta}(t) = \frac{\dot{\gamma}}{2} \frac{(\lambda \sin 2\phi) \sqrt{(\lambda \cos 2\phi + 1)C^2(1 + \lambda)}}{[(\lambda \cos 2\phi + 1) + C^2(1 + \lambda)]}, \\ \dot{\psi}(t) = -\frac{\dot{\gamma}}{2} (\lambda \cos 2\phi) \cos \theta$$

Where scalar magnitude of the strain rate tensor $\dot{\gamma}$ is given as

$$\lambda = \frac{r_e^2 - 1}{r_e^2 + 1}, \qquad \dot{\gamma} = \sqrt{\frac{1}{2} \underline{\Gamma}} \underline{\Gamma}, \qquad \underline{\Gamma} = \frac{1}{2} \left[\left(\underline{\nabla} \underline{U} \right) + \left(\underline{\nabla} \underline{U} \right)^T \right]$$

 $\underline{\underline{\Gamma}}$ is the second-order rate of deformation tensor and $\underline{\nabla U}$ is the velocity gradient tensor. For simple shear in one plane $C=+\infty$ such that $\theta=\pi/2$, $\psi=0, \dot{\psi}=\dot{\theta}=0$. Jeffery's Orbital period is given as

$$T = \frac{2\pi}{\dot{r}} [r_e + \frac{1}{r_e}]$$
 15

Results of the 2D simulation using similar input data were obtained from [8]. The results below show slight deviation in tumbling period especially for the 3D model. Further mesh refinement would be required for close exact match however at a computational cost.

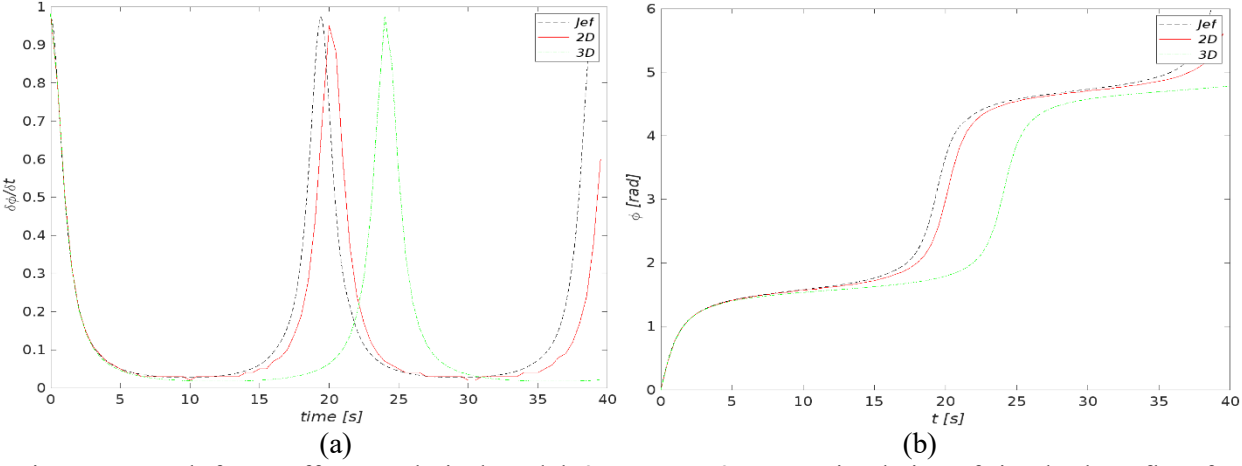


Figure 7: Result from Jeffery Analytical model, 2D FEA & 3D FEA simulation of simple shear flow for (a) In-plane angular velocity (b) In plane orientation angle.

The result of the 3D simulation for the case of simple shear shows a drop in the minimum pressure on the fiber surface along Jefferies orbit to about -13kPa below the far-field reference pressure of 0kPa set at the start of the analysis (cf. Figure 8(a)). Based on our hypothesis, the pressure dip suggests a propensity for the onset of void nucleation at these sites where they occur (cf. Figure 8(b)).

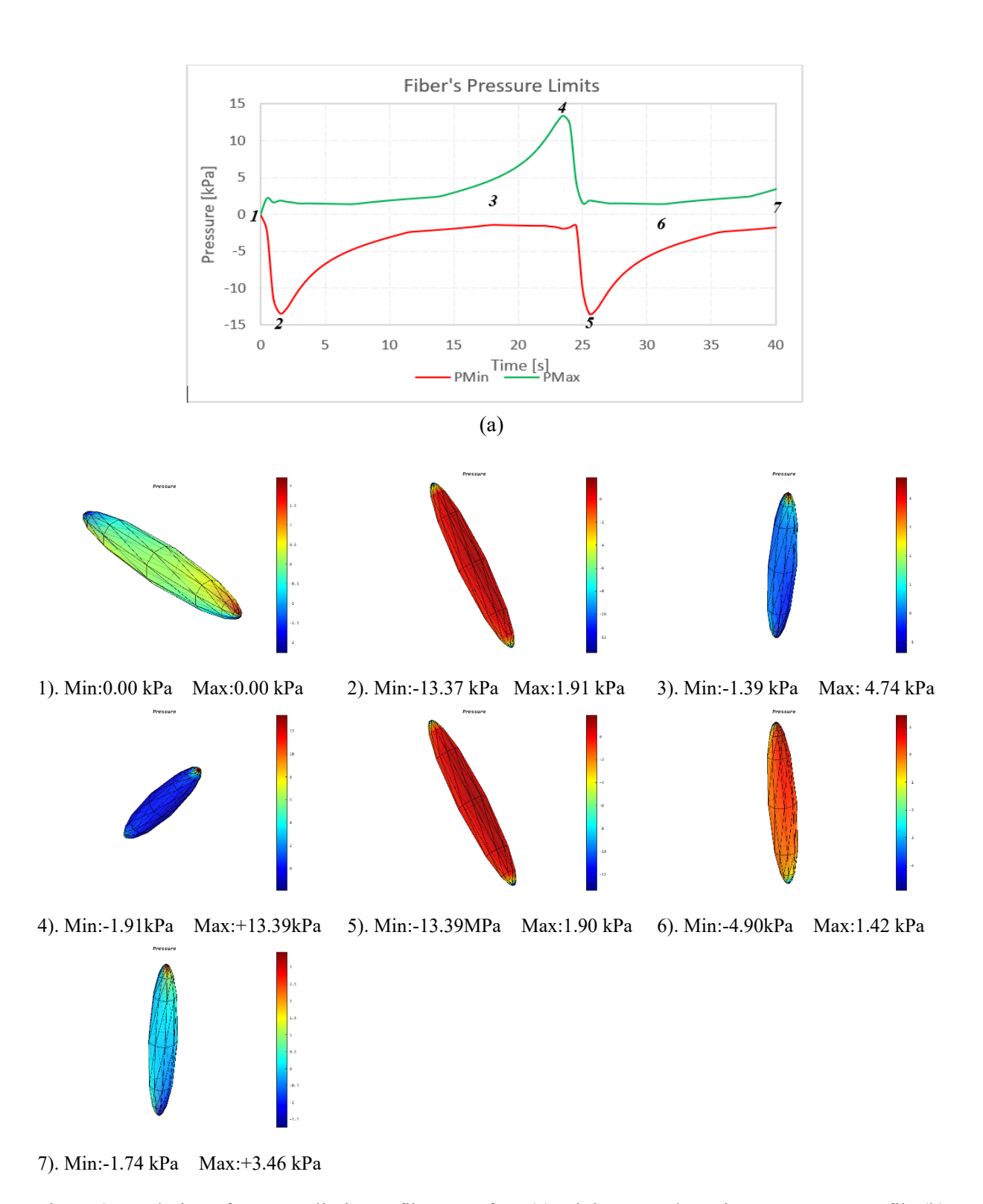


Figure 8: Evolution of pressure limits on fiber's surface (a) minimum and maximum pressure profile (b) Surface Contour at different time stamps.

Results & Discussion

Subsequent results presented in this section are based on actual 3D streamline data (velocity, velocity gradients, and pressure) obtained from the BAAM extrusion deposition flow model (cf. Figure 3). The fiber's evolution analysis is carried out for 2 streamlines, streamline ψ =4 closer to the nozzle center and ψ =20 closer to the nozzle edge. At the nozzle center, the velocity gradients are not as severe compared to streamlines closer to the nozzle edge (cf. Figure 2(c)). As expected, we do not experience high rotational velocities for streamlines closer to the center compared to those farther out especially at the region where the fiber' exits the nozzle and turns onto the bed due to relatively lower shear rates (cf. Figure 14 (a, c)). It is worth noting that the deposition times however for the edge streamlines are relatively longer (about 9.7s for ψ =20) compared to the center streamline due to the wall effect (about 5.7s for ψ =4). Thus, the translational velocities are higher for the streamlines closer to the center ψ =4, than for those closer to the nozzle edge (cf. Figure 14 (b, d)).

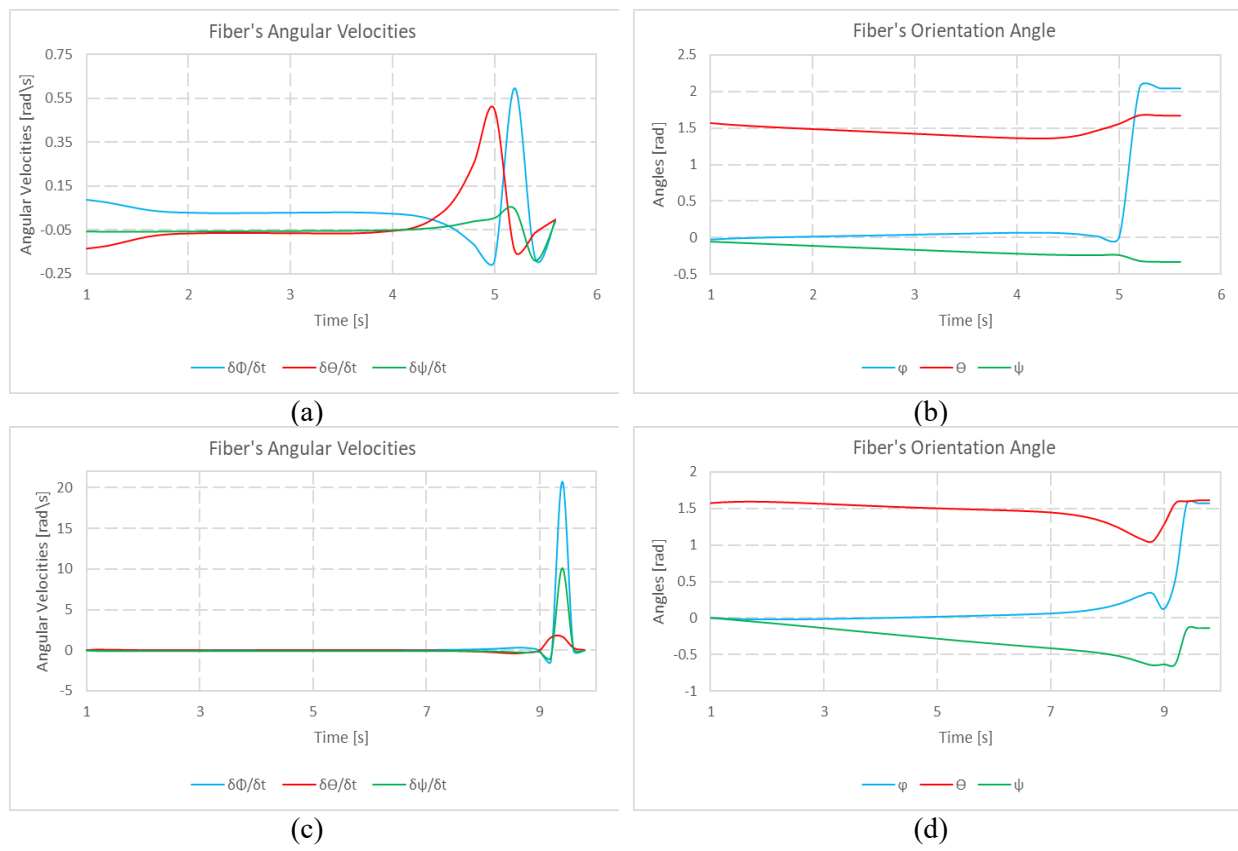


Figure 9: Evolution of fiber's angular velocity for (a) streamline ψ =4 (c) streamlines ψ =20, and Evolution of fiber's orientation angle for (b) streamline ψ =4 (d) streamlines ψ =20

The results for the pressure limits on the fibers surface for both streamlines shows that the fiber pressure persists below the reference pressure during the downward travel however at the region of interest where it exits the nozzle and is deposited on the bed, the minimum pressure stays well below the reference pressure for the streamline closer to the edge (ψ =20) about -0.4Mpa, however this is not the case for streamline 4 closer to the center where the minimum pressure goes above the reference pressure before it returns to the zero (cf. Figure 9 (a, b))

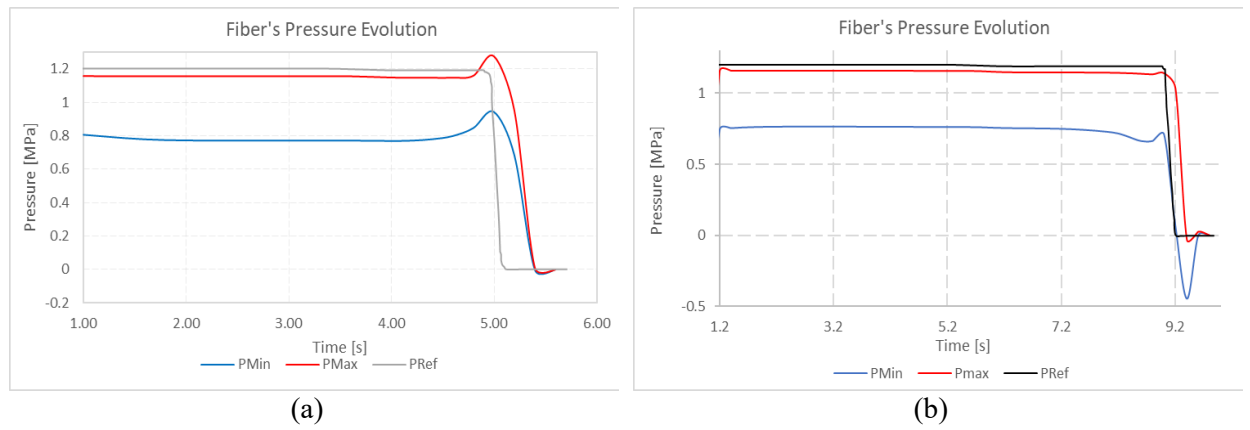


Figure 10: Evolution of Pressure limits on fiber's surface for (a) streamline ψ =4 (b) streamlines ψ =20

Conclusion

The paper presents preliminary investigation on localized pressure related void nucleation during polymer extrusion/deposition flow process based on 3D simulation to study the impact of out-of-plane fiber orientation on void nucleation propensity at these low-pressure sites. Currently, we do not have established benchmark to understand the effect of out of plane 3D orientation on the pressure response, however we report substantial drop in the minimum pressure as the fiber exits the nozzle for streamlines closer to the edge with higher velocity gradients compared to those closer to the center which are pointers to likelihood for void formation [1,18]. We see from the results that for most part during the deposition, the fiber's pressure stays below the far field pressure.

Work is currently underway to establish a relationship between print processing parameters and likelihood of void formation and to improve simulation calculation efficiency and accuracy. Other factors that could significantly impact the pressure response on the fiber surface such as non-Newtonian fluid behavior, initial fiber orientation, fiber-fiber interaction, and flexure consideration of the fiber suspension for high aspect ratio fibers would be considered for further investigation.

References

- 1. Roychowdhury, S., Gillespie Jr, J.W. and Advani, S.G., 2001. Volatile-induced void formation in amorphous thermoplastic polymeric materials: I. Modeling and parametric studies. *Journal of composite materials*, 35(4), pp.340-366.
- 2. Vaxman, A., Narkis, M., Siegmann, A. and Kenig, S., 1989. Void formation in short-fiber thermoplastic composites. Polymer composites, 10(6), pp.449-453.
- 3. Yang, D., Zhang, H., Wu, J. and McCarthy, E.D., 2021. Fibre flow and void formation in 3D printing of short-fibre reinforced thermoplastic composites: An experimental benchmark exercise. Additive Manufacturing, 37, p.101686.
- 4. Jeffery, G. B. The motion of ellipsoidal particles immersed in a viscous fluid. Proceedings of the Royal Society of London. Series A, 102(715):161-179, 1922.
- 5. Bertevas E, Férec J, Khoo B C, et al. Smoothed particle hydrodynamics (SPH) modeling of fiber orientation in a 3D printing process[J]. Physics of Fluids, 2018, 30(10): 103103.
- 6. Heller, B.P., Smith, D.E. and Jack, D.A., 2019. Planar deposition flow modeling of fiber filled composites in large area additive manufacturing. Additive Manufacturing, 25, pp.227-238.
- 7. Ouyang Z, Bertevas E, Parc L, et al. A smoothed particle hydrodynamics simulation of fiber-filled composites in a non-isothermal three-dimensional printing process[J]. Physics of Fluids, 2019, 31(12): 123102.
- 8. Wang, Z. and Smith, D.E., 2021. A Fully Coupled Simulation of Planar Deposition Flow and Fiber Orientation in Polymer Composites Additive Manufacturing. Materials, 14(10), p.2596.
- 9. Awenlimobor, A., Wang, Z. and Smith, D.E., 2021. Physical Modeling: Simulation of Micro-Void Development within Large Scale Polymer Composite Deposition Beads. In 2021 International Solid Freeform Fabrication Symposium. University of Texas at Austin.
- 10. Rajaguru, K., Karthikeyan, T. and Vijayan, V., 2020. Additive manufacturing–State of art. Materials today: proceedings, 21, pp.628-633.
- 11. Van de Werken, N., Tekinalp, H., Khanbolouki, P., Ozcan, S., Williams, A. and Tehrani, M., 2020. Additively manufactured carbon fiber-reinforced composites: State of the art and perspective. Additive Manufacturing, 31, p.100962.
- 12. Mehdikhani, M., Gorbatikh, L., Verpoest, I. and Lomov, S.V., 2019. Voids in fiber-reinforced polymer composites: A review on their formation, characteristics, and effects on mechanical performance. Journal of Composite Materials, 53(12), pp.1579-1669.
- 13. Wang, Z., 2019. Computational Modeling of Fiber Reinforced Composites Melt Flow in Nozzle Extrudate for Polymer Deposition Additive Manufacturing (Doctoral dissertation, Baylor University).
- 14. Zhang, D. and Smith, D.E., 2016. Dynamic simulation of discrete fiber motion in fiber-reinforced composite materials processing. Journal of Composite Materials, 50(10), pp.1301-1319.
- 15. Zhang, D. and Smith, D.E., 2015. Finite element-based brownian dynamics simulation of nanofiber suspensions using Monte Carlo Method. Journal of Micro and Nano-Manufacturing, 3(4).
- 16. Fallon, J.J., McKnight, S.H. and Bortner, M.J., 2019. Highly loaded fiber filled polymers for material extrusion: A review of current understanding. Additive Manufacturing, 30, p.100810.
- 17. Reddy, J.N., 2019. Introduction to the finite element method. McGraw-Hill Education.
- 18. Han, J.H. and Dae Han, C., 1990. Bubble nucleation in polymeric liquids. II. Theoretical considerations. Journal of Polymer Science Part B: Polymer Physics, 28(5), pp.743-761.